Energy and AI 14 (2023) 100278

Contents lists available at ScienceDirect

Energy and AI

journal homepage: www.sciencedirect.com/journal/energy-and-ai

Long short-term memory deep learning model for predicting the dynamic performance of automotive PEMFC system

Bowen Wang [a,b,e,1], Zijun Yang [a,1], Mingxi Ji [c,1], Jing Shan [d], Meng Ni [b,*], Zhongjun Hou [d,*], Jun Cai [d], Xin Gu [d], Xinjie Yuan [d], Zhichao Gong [a], Qing Du [a,e], Yan Yin [a,e], Kui Jiao [a,e,*]

[a] State Key Laboratory of Engines, Tianjin University, 135 Yaguan Rd, Tianjin 300350, China
[b] Department of Building and Real Estate, Research Institute for Sustainable Urban Development (RISUD), Research Institute for Smart Energy (RISE), The Hong Kong Polytechnic University, Hung Hom, Kowloon, Hong Kong, China
[c] Birmingham Centre for Energy Storage, University of Birmingham, Edgbaston, Birmingham, B15 2TT, United Kingdom
[d] Shanghai Hydrogen Propulsion Technology Co., Ltd., Unit 10, BLDG 17, Innovation Park, Lane 56, Antuo Rd. Jiading, Shanghai China
[e] National Industry-Education Platform of Energy Storage, Tianjin University, Tianjin, China

HIGHLIGHTS

- A LSTM deep learning model for predicting dynamic performance of PEMFC is proposed.
- Dynamic process of automotive PEMFC is generated by the system-level simulation.
- A content predictive performance is achieved based on the proposed model.
- Input feature selection, sequence duration and sampling frequency are optimized.

GRAPHICAL ABSTRACT

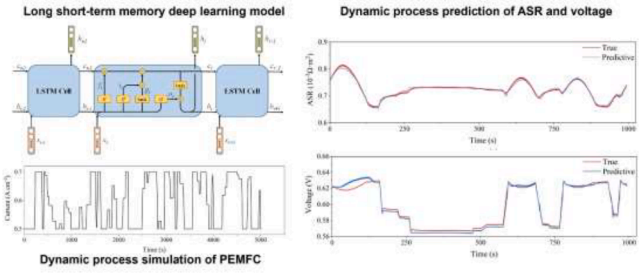

ARTICLE INFO

Keywords:
Automotive PEMFC
Long short-term memory neural network
Dynamic process
Output voltage
Area specific resistance

ABSTRACT

As a high efficiency hydrogen-to-power device, proton exchange membrane fuel cell (PEMFC) attracts much attention, especially for the automotive applications. Real-time prediction of output voltage and area specific resistance (ASR) via the on-board model is critical to monitor the health state of the automotive PEMFC stack. In this study, we use a transient PEMFC system model for dynamic process simulation of PEMFC to generate the dataset, and a long short-term memory (LSTM) deep learning model is developed to predict the dynamic performance of PEMFC. The results show that the developed LSTM deep learning model has much better performance than other models. A sensitivity analysis on the input features is performed, and three insensitive features are removed, that could slightly improve the prediction accuracy and significantly reduce the data volume. The neural structure, sequence duration, and sampling frequency are optimized. We find that the optimal sequence data duration for predicting ASR is 5 s or 20 s, and that for predicting output voltage is 40 s. The sampling frequency can be reduced from 10 Hz to 0.5 Hz and 0.25 Hz, which slightly affects the prediction accuracy, but obviously reduces the data volume and computation amount.

* Corresponding authors.
E-mail addresses: meng.ni@polyu.edu.hk (M. Ni), hou_zhongjun@shpt.com (Z. Hou), kjiao@tju.edu.cn (K. Jiao).
[1] Equal contribution

https://doi.org/10.1016/j.egyai.2023.100278

Available online 17 June 2023
2666-5468/© 2023 The Authors. Published by Elsevier Ltd. This is an open access article under the CC BY-NC-ND license (http://creativecommons.org/licenses/by-nc-nd/4.0/).

Nomenclature

A	Area (m^2)
ASR	Area specific resistance (Ω m^2)
b	Biases
c	Molar concentration of gas component (mol m^{-3}); Cell state
c_p	Specific heat (J kg^{-1} K^{-1})
C_f	Friction factor
e	Deviation (bar), Natural constant
E_{rev}	Reversible potential (V)
f	Forget gate
F	Faraday constant (C mol^{-1})
g	Updated value of cell state
h	Hidden state
i	Input gate
I	Current density (A m^{-2})
J	Rotational inertia (kg m^2)
K_p, K_I, K_D	PID control coefficients
L	Length (m)
m	Mass flowrate (kg s^{-1})
M	Molar weight (g mol^{-1})
N	Rotational speed (RPM)
o	Output gate
p	Power (W)
Δp	Total pressure loss (Pa)
Δp_m	Local pressure loss (Pa)
Δp_f	Frictional pressure loss (Pa)
P	Pressure (bar, Pa)
R	Universal gas constant (J K^{-1} mol^{-1}); Motor resistance (Ω)
t_{pip}	Transmission time of gas in the pipeline (s)
T	Temperature (K)
u	Velocity (m s^{-1}), Change of control voltage (V)
V	Voltage (V)
W	Volume flowrate (m^3 h^{-1}); Weight
x	Rotational speed after data standardization processing; Input vector
X	Molar fraction
y	Mass fraction; Volume flowrate after data standardization processing
α	Charge transfer coefficient
γ	Specific heat ratio
ρ	Density (kg m^{-3})
δ	Thickness (m)
δ_{pip}	Hydraulic diameter of the pipeline (m)
η	Efficiency
η_{ohm}	Ohmic loss (V)
η_{act}	Activation loss (V)
σ_s	Electronic conductivity (S m^{-1})
σ_m	Ionic conductivity (S m^{-1})
σ_N	Standard deviation of rotational speed
σ_W	Standard deviation of volume flowrate
μ	Dynamic viscosity (kg m^{-1} s^{-1})
ν	Control voltage, V
τ	Torque (N m)
ω	Angular velocity (rad s^{-1})
μ	Dynamic viscosity (kg m^{-1} s^{-1})
μ_N	Average value of rotational speed (RPM)
μ_W	Average value of volume flowrate (m^3 h^{-1})

Superscript and subscript

a	Anode
ave	Average
ACL	Anode catalyst layer
BP	Bipolar plate
bc	Corrected state of hydrogen pump
bl	Actual state of hydrogen pump
bm	Motor
c	Cathode
cool	Coolant
CCL	Cathode catalyst layer
CL	Catalyst layer
eff	Effective value
f	Forget gate
GDL	Gas diffusion layer
H_2	Hydrogen
in	Inlet
MPL	Micro-porous layer
O_2	Oxygen
pip	Pipeline
ref	Reference value
t-1	The previous time step
t	The current time step

1. Introduction

Since the industrial revolution, machine gradually took the place of manpower, and human demand for energy was increasing day by day. From wood to oil, from low calorific value fuel to high calorific value fuel, human beings consume a large amount of fossil energy. A large amount of greenhouse gasses such as CO_2 is emitted, causing global warming, which is recognized as the culprit of frequent extreme weather [1]. Many countries have put forward carbon neutrality goals and accelerate the development of hydrogen energy industry chain in their technical routes [2]. Proton exchange membrane fuel cell (PEMFC), which converts hydrogen to power, has the advantages of zero emission, high energy conversion efficiency, no mechanical vibration and low noise, and thus it is widely regarded as a promising propulsion in the automotive field [3–8].

Dynamic prediction of the PEMFC performance and internal state is critical to monitor the health state of the automotive PEMFC stack. Since the analytical model is inaccurate in reflecting the characteristics of the PEMFC compared with the actual system performance, it is of great significance to establish a dynamic mathematical model of the PEMFC with high robustness [9]. Mathematical models have been widely used in the performance prediction and analysis of the PEMFC, which can be divided into physical models [10–14] and data-driven models [15–17]. Physical models are developed based on the basic physical and chemical processes inside the PEMFC and solve the complex coupled governing equations. Thus, the physical models generally are more accurate but more complex and computationally demanding. In contrast, the data-driven modeling focuses on finding the input-output relationships from experimental datasets collected from the operation of a fuel cell system, without the in-depth knowledge of these physical and chemical processes, resulting in high computational efficiency. This characteristic makes data-driven models extremely important in the on-board automotive applications, which usually involve complex systems, dynamic variation, and long-term operation. The data-driven model represented by machine learning can greatly help to expand the application of complex physical models due to its high prediction accuracy and computational efficiency. Using the simulation data of complex physical models to train machine learning models is a popular method, commonly known as the surrogate modeling [15]. Wang et al. [18] developed a 3D computational fluid dynamics (CFD) PEMFC model with

Table 1
Regression coefficient of the characteristic curve of hydrogen circulation pump.

Coefficient	Value
a_0	1.4271
a_1	0.3671
a_2	0.4356
a_3	0.0588
a_4	0.1272
a_5	0.0745

catalyst layer (CL) agglomerate model, and then used the model to build a PEMFC performance database with various CL compositions. The database was used to train the data-driven surrogate model based on support vector machine (SVM), and the developed surrogate model showed comparable accuracy with the physical model. This surrogate model could give a polarization curve within 1 s, while the CFD model would take hundreds of hours. Moreover, the surrogate model was fed into the genetic algorithm (GA) to obtain the optimal CL composition. In order to verify the correctness, they input the optimal CL composition into the physical model, and the percentage error between the maximum power density predicted by the surrogate model and that calculated by the physical model was only 1.395%. Qiu et al. [19] trained a radial basis function neural network (RBFNN) model through the dataset generated by a finite element (FE) model of a full-scale single PEMFC. Then, the RBFNN model was fed into GA to obtain the optimal reactor clamping mode, and the clamping mode was input into the FE model for validation. The results showed that the uniformity of contact pressure on the GDL was greatly improved. Li et al. [20] established a 3D steady-state CFD model of the PEMFC as the basic model for optimization, and then used variance analysis to select 6 parameters, operating pressure, operating temperature, anode stoichiometry, GDL thickness, membrane thickness and channel width, that had significant effects on the performance of the PEMFC from 11 commonly used parameters. Three ensemble learning models were used to train the surrogate models. Finally, three PEMFC performance indexes, power density, efficiency, and oxygen distribution uniformity in the CL, are optimized simultaneously based on non-dominated sorting genetic algorithm-II (NSGA-II). The results showed that the PEMFC model with optimal parameters was better than the original model in all three performance indexes. Yang et al. [21] built a quasi-2D model of the PEMFC to generate the dynamic performance data of dead-ended anode (DEA) and anode recirculation operations. They proposed a surrogate model combining the multivariate polynomial regression (MPR) method and artificial neural network (ANN) approach to quickly predict the short-term degradation behaviors of PEMFC and discussed the influence of the number of hidden layers and the activation function on the prediction curve.

Based on the literature review, data-driven surrogate models are mainly used to predict and optimize the PEMFC performance. The physical quantities inside the PEMFC can directly reflect the current state and durability of the PEMFC. For example, area specific resistance (ASR), which can directly reflect the membrane water content, is a key physical parameter to evaluate the dryness or flooding of PEMFC. However, the instrument used to measure the ASR is expensive and impractical, so it is very useful to estimate the ASR from the easily measured operating conditions and physical quantities, which can monitor the operation state of the automotive PEMFC stack in real time. Therefore, the main purpose of this study is to use deep learning algorithm to replace the existing physical model, and to obtain a deep learning surrogate model with reliable results and fast calculation efficiency. We use the easily measured operating conditions and physical quantities as the input, and use the surrogate model based on long short-term memory (LSTM) to predict the ASR and output voltage of PEMFC. The surrogate model is used to perform sensitivity analysis on the input features, based on which, multiple input features are effectively removed. Then, we search for the optimal input data sequence duration to reduce the sampling frequency, reduce the complexity of the surrogate model and the size of the input data.

Table 2
Parameters of hydrogen circulation pump model.

Parameter	Value
Rotational inertia of blower, J_{bl}	2.6×10^{-3} kg m^2
Torque constant of motor, κ_t	0.15 N mA^{-1}
Voltage constant of motor, κ_v	0.15 V s rad^{-1}
Efficiency of motor, η_{bm}	0.9
Efficiency of hydrogen circulation pump, η_{bl}	0.8
Motor resistance, R_{bm}	0.82 Ω
Reference temperature, T_{ref}	288 K
Reference pressure, P_{ref}	1 bar
Proportional coefficient, K_p	2.842
Integral coefficient, K_I	232.770
Differential coefficient, K_D	1.854

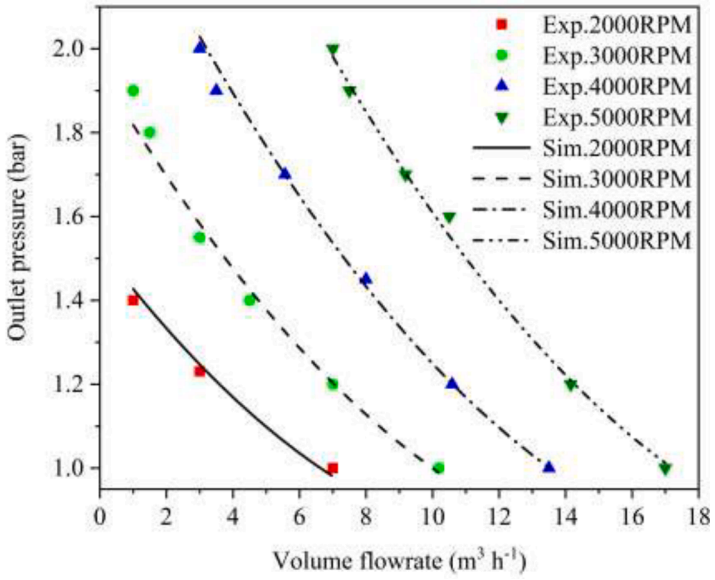

Fig. 1. The characteristic curve of the hydrogen circulation pump [23] and the fitting result.

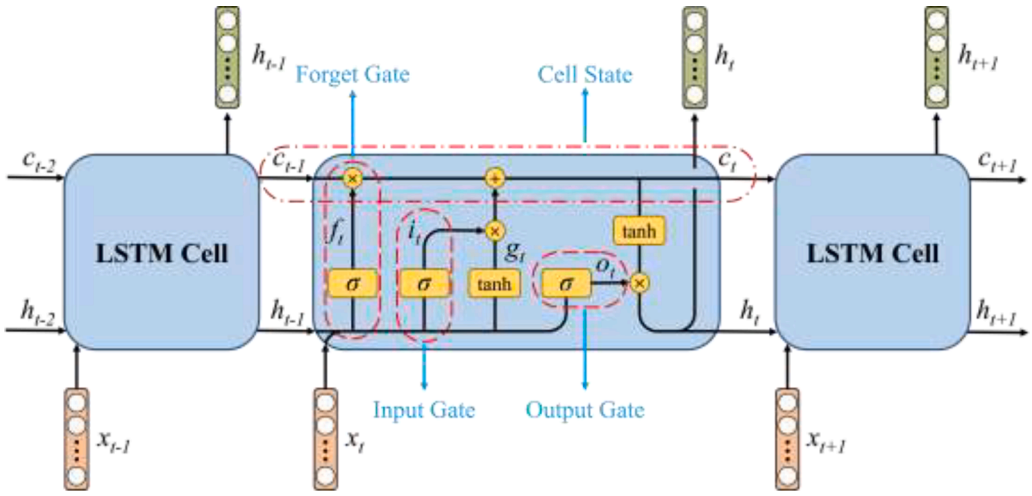

Fig. 2. Schematic of LSTM model.

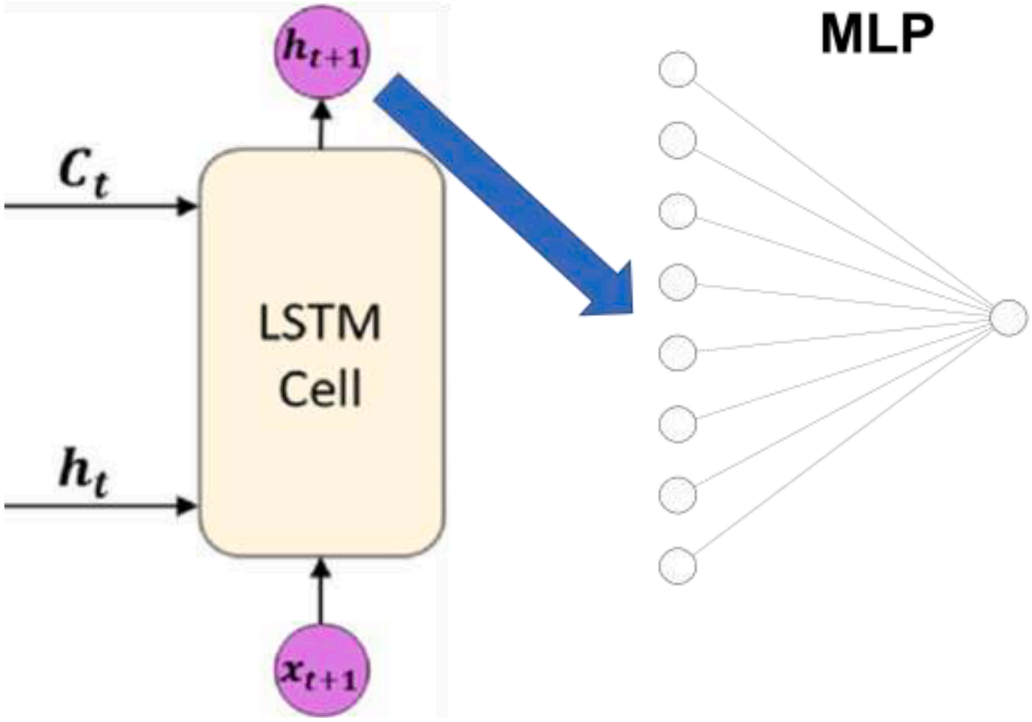

Fig. 3. Schematic of the core concepts of LSTM.

Table 3
Performance comparison of three algorithms for predicting the ASR and output voltage in operating condition 1.

Parameter	Algorithm	R^2	MAE	RMSE	MAPE
ASR	MPR	0.4412	0.0189	0.0250	2.5624
	SVR	0.7740	0.0136	0.0159	1.8868
	LSTM-MLP	0.9829	0.0034	0.0044	0.4710
Output voltage	MPR	0.9655	0.0036	0.0046	0.5916
	SVR	0.9623	0.0036	0.0048	0.5939
	LSTM-MLP	0.9819	0.0026	0.0033	0.4437

Table 4
Comparative performance of LSTM-MLP with different network structures for ASR and output voltage prediction.

Parameter	network structure	R^2	MAE	RMSE	MAPE
ASR	8–1	0.9983	0.0014	0.0019	0.1916
	8–8–1	0.9985	0.0012	0.0018	0.1743
	16–8–1	0.9982	0.0013	0.0019	0.1880
	32–8–1	0.9980	0.0015	0.0020	0.2037
	64–32–8–1	0.9979	0.0015	0.0021	0.2155
Output voltage	8–1	0.9950	0.0012	0.0018	0.2001
	8–8–1	0.9953	0.0012	0.0018	0.1881
	16–8–1	0.9954	0.0011	0.0017	0.1857
	32–8–1	0.9945	0.0013	0.0019	0.2108
	64–32–8–1	0.9952	0.0012	0.0018	0.1881

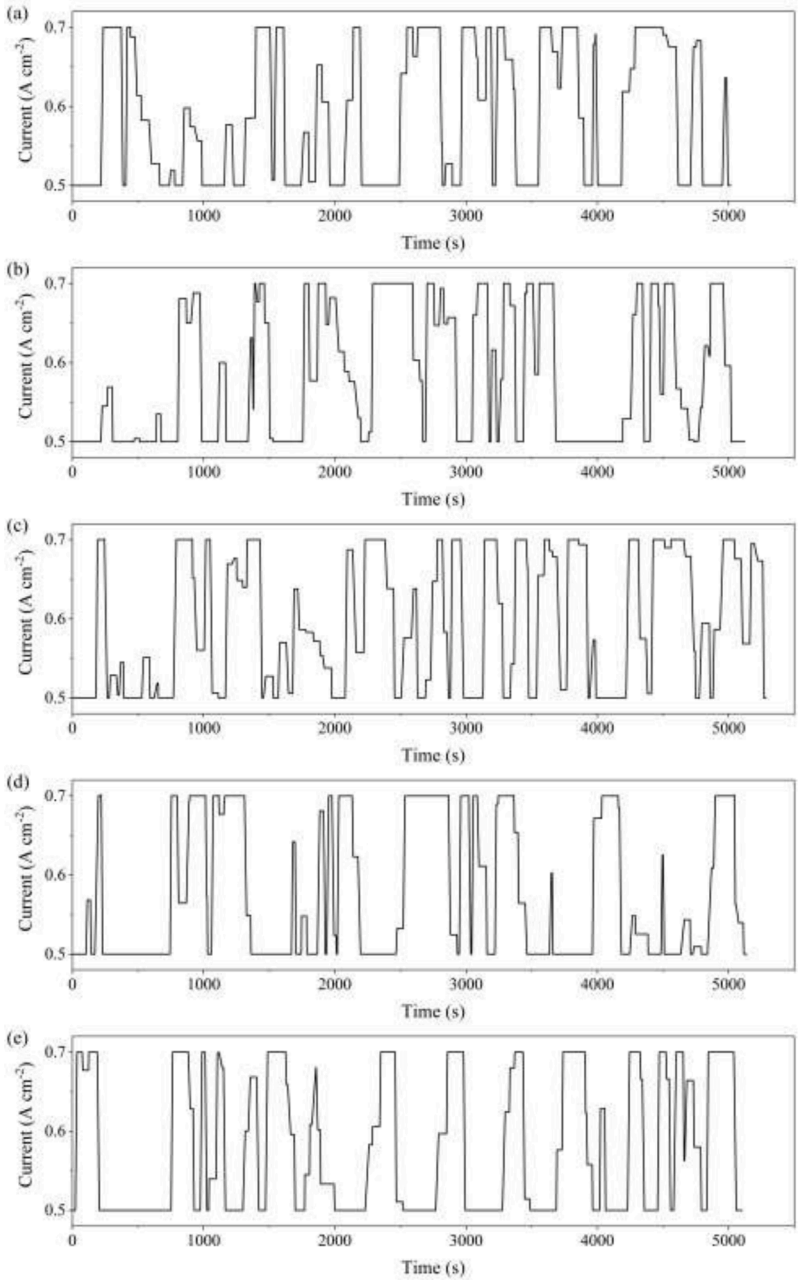

Fig. 4. Five generated random operating conditions of automotive PEMFC: (a) operating condition 1, (b) operating condition 2, (c) operating condition 3, (d) operating condition 4, (e) operating condition 5.

2. Methods

2.1. PEMFC system model development

The automotive PEMFC system generally consists of the PEMFC stack and water and heat auxiliaries, including the air compressor, hydrogen circulation pump, membrane humidifier, radiator, and pipeline network.

2.1.1. Quasi-2D PEMFC model

The previously developed quasi-2D PEMFC model is employed in this study [22]. The polarization curve directly determines the output performance of PEMFC. The calculation formula of output voltage is:

$$V = E_{\text{rev}} - \eta_{\text{ohm}} - \eta_{\text{act}} \tag{1}$$

where V (V) is the output voltage; E_{rev} (V) is the reversible potential; η_{ohm}(V) is the ohmic loss; η_{act}(V) is the activation loss. The reversible voltage follows the thermodynamics and is the ideal maximum output voltage of the fuel cell, which is expressed by Nernst equation:

$$E_{\text{rev}} = 1.229 - 2.304 \times 10^{-4}(T - 298.15) + \frac{RT}{2F}\left[ln\left(P_{\text{H}_2,\text{in}}\right) + \frac{1}{2}ln\left(P_{\text{O}_2,\text{in}}\right)\right] \tag{2}$$

where R (8.314 J mol^{-1} K^{-1}) is the universal gas constant; T (K) is the temperature; F (96,485 C mol^{-1}) is the Faraday constant; P (bar) is the pressure. The superscripts and subscripts: H_2 represents hydrogen; O_2 represents oxygen; in represents inlet. Ohmic loss is caused by the resistance of ions or electrons in different components of the cell, and can be calculated as:

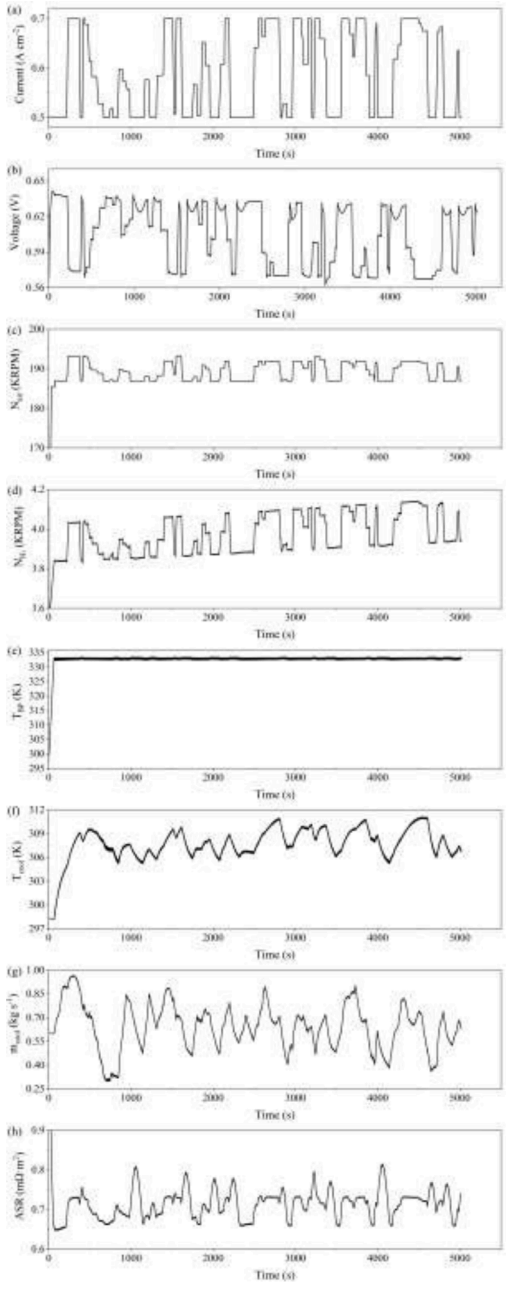

Fig. 5. Data set and parameters of operating condition 1: (a) current density, (b) single cell output voltage, (c) air compressor rotational speed, (d) hydrogen circulation pump rotational speed, (e) bipolar plate temperature, (f) coolant outlet temperature, (g) coolant flow rate, (h)ASR.

$$\eta_{ohm} = I{\cdot}ASR = I\left(\frac{\delta_{BP}}{\sigma_{s,BP}} + \frac{\delta_{GDL}}{\sigma^{eff}_{s,GDL}} + \frac{\delta_{MPL}}{\sigma^{eff}_{s,MPL}} + \frac{\delta_{CL}}{2\sigma^{eff}_{s,CL}} + \frac{\delta_{CL}}{2\sigma^{eff}_{m,CL}} + \frac{\delta_m}{\sigma_m}\right) \tag{3}$$

where I (A m^2) is the current density; δ (m) is the thickness; σ_s and σ_m (S m^{-1}) are the electronic and ionic conductivities, respectively. The superscripts and subscript: eff represents effective value, BP represents bipolar plate; GDL represents gas diffusion layer; MPL represents microporous layer; CL represents catalyst layer. The activation loss can be calculated by the Tafel equation:

$$\eta_{act} = \frac{RT}{2\alpha F}\ln\left(\frac{I}{j_a\delta_{ACL}\left(\frac{c_{H_2,ACL}}{c^{ref}_{H_2}}\right)}\right) + \frac{RT}{4\alpha F}\ln\left(\frac{I}{j_c\delta_{CCL}\left(\frac{c_{O_2,CCL}}{c^{ref}_{O_2}}\right)}\right) \tag{4}$$

where α is the charge transfer coefficient; j (A m^{-3}) is the reaction rate; c (mol m^{-3}) is the molar concentration of gas components. The superscripts and subscripts: a represents anode; c represents cathode; ACL represents anode catalyst layer; CCL represents cathode catalyst layer; ref represents reference.

The heat and mass transfer equations and the parameters of the simulated PEMFC could be found in Ref. [22].

2.1.2. Hydrogen circulation pump model

Hydrogen circulation pump is an important component of the PEMFC system. It not only improves the utilization of fuel, but also humidifies hydrogen by recirculating water vapor. The volume flowrate of gas at the inlet of hydrogen circulation pump, the angular velocity and rotational speed are corrected as follows:

$$W_{bc} = W_{bl}\frac{\sqrt{T_{in}/T_{ref}}}{P_{in}/P_{ref}}, \omega_{bc} = \frac{\omega_{bl}}{\sqrt{T_{in}/T_{ref}}}, N_{bc} = \frac{N_{bl}}{\sqrt{T_{in}/T_{ref}}} \tag{5}$$

where W (m^3 h^{-1}) is the volume flowrate; ω (rad s^{-1}) is the angular velocity; N (RPM) is the rotational speed. The subscripts: bc and bl represent corrected and actual states of hydrogen pump, respectively. The sample points in the characteristic curve of hydrogen circulation pump are standardized to fit the curve:

$$x = \frac{N_{bc} - \mu_N}{\sigma_N}, y = \frac{W_{bc} - \mu_W}{\sigma_W} \tag{6}$$

where x and y are the rotational speed and volume flowrate after data standardization processing, respectively; μ_N (RPM) and μ_W (m^3 h^{-1}) are the average values of rotational speed and volume flowrate of sample points, respectively; σ_N and σ_W are the standard deviation of the rotational speed and volume flowrate of the sample point, respectively.

The relationship between volume flowrate, rotational speed and outlet pressure of hydrogen circulation pump is fitted by using second order equation [23]. This process is done by using the scikit-learn library of the interpreted programming language Python. The second order equation is as follows:

$$P_{out} = a_0 + a_1x + a_2y + a_3x^2 + a_4xy + a_5y^2 \tag{7}$$

where P_{out} (bar) is the outlet pressure of hydrogen circulation pump; a_0, a_1, a_2, a_3, a_4, a_5 are regression coefficients. The values of coefficients are shown in Table 1. The coefficient of determination of the fitting result is 0.9923, which shows that the good fitting performance (as shown in Fig. 1 [23]).

The hydrogen pump is driven by motor and the inertance of drive motor is calculated as:

$$\frac{d\omega_{bl}}{dt} = \frac{1}{J_{bl}}(\tau_{bm} - \tau_{bl}) \tag{8}$$

$$\tau_{bm} = \eta_{bm}\frac{\kappa_t}{R_{bm}}(v_{bm} - \kappa_v\omega_{bl}) \tag{9}$$

$$\tau_{bl} = \frac{p_{bl}}{\omega_{bl}} \tag{10}$$

$$p_{bl} = c_{p,in}\frac{T_{in}}{\eta_{bl}}\left[\left(\frac{P_{out}}{P_{in}}\right)^{\frac{\gamma_{g,in}-1}{\gamma_{g,in}}} - 1\right]m_{in} \tag{11}$$

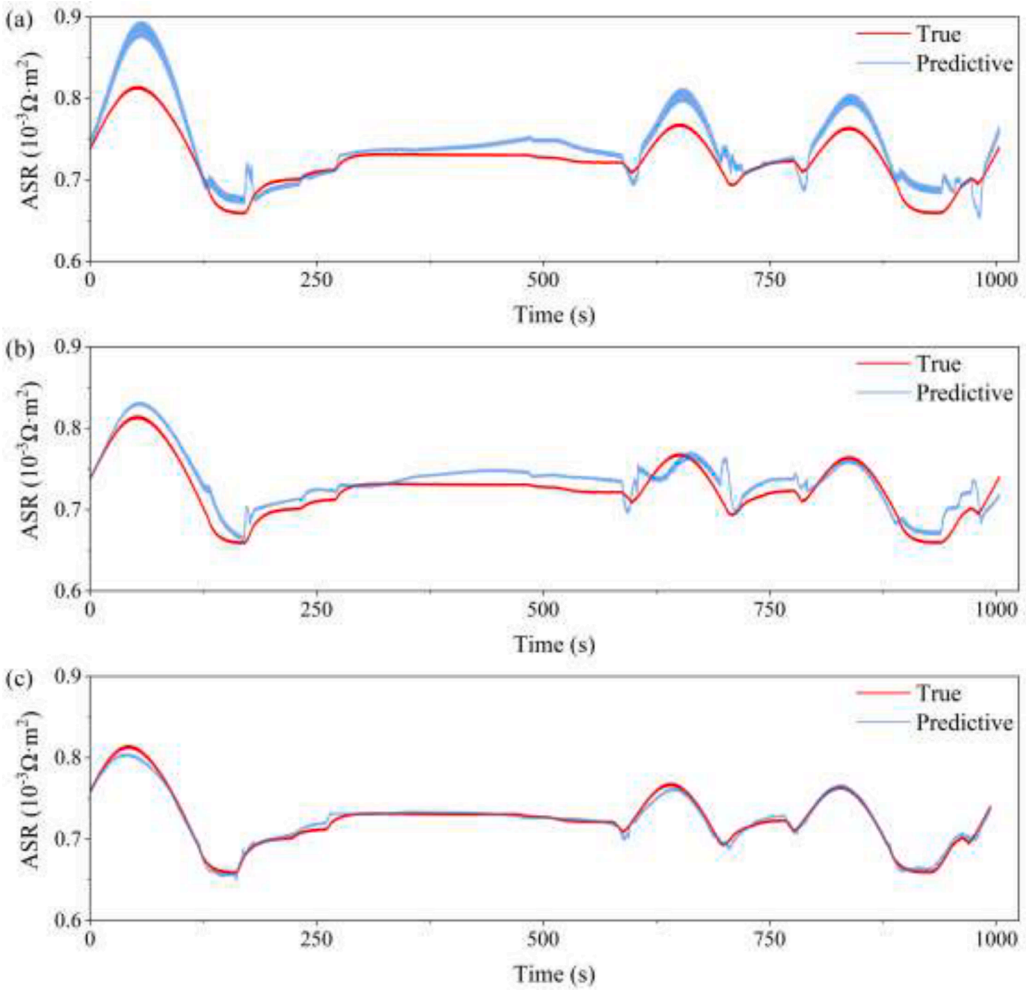

Fig. 6. Prediction results of ASR in operating condition 1: (a) MPR, (b) SVR, (c) LSTM-MLP.

$$c_{p,in} = c_{p,H_2} y_{H_2,in} + c_{p,v} y_{v,in} + c_{p,N_2} y_{N_2,in} \tag{12}$$

$$\gamma_{g,in} = \gamma_{H_2} y_{H_2,in} + \gamma_v y_{v,in} + \gamma_{N_2} y_{N_2,in} \tag{13}$$

$$T_{out} = T_{in} + \frac{T_{in}}{\eta_{bl}} \left[\left(\frac{P_{out}}{P_{in}} \right)^{\frac{\gamma_{g,in}-1}{\gamma_{g,in}}} - 1 \right] \tag{14}$$

$$v_{bm} = \kappa_v \omega_{bl} + \frac{p_{bl} R_{bm}}{\omega_{bl} \eta_{bm} \kappa_t} \tag{15}$$

where J (kg m^2) is the rotational inertia; τ (N m) is the torque; p (W) is the power; η is the efficiency; R (Ω) is the motor resistance; v (V) is the control voltage for motor; bl and bm represent the state of load (hydrogen pump) and motor, respectively, $c_{p,in}$ (J kg^{-1} K^{-1}) is the specific heats with a constant pressure of the inlet gas; P_{in} (bar) is the inlet pressure of hydrogen circulation pump; $\gamma_{g,in}$ is the specific heat ratio of the inlet gas; m_{in} (kg s^{-1}) is the mass flowrate of the inlet gas; $y_{H_2,in}$, $y_{v,in}$ and $y_{N_2,in}$ are the mass fractions of hydrogen, water vapor, and nitrogen in the inlet gas, respectively; T_{out} (K) is the temperature of the outlet gas.

The calculated actual outlet pressure is compared with the target outlet pressure, and then the difference between the two is used as the deviation of the proportional-integral-derivative (PID) control, to calculate the change of the control voltage:

$$e(t) = P_{tar} - P_{out} \tag{16}$$

$$u(t) = K_p e(t) + K_I \int e(t)dt + K_D \frac{de(t)}{dt} \tag{17}$$

$$v_{bm,new} = v_{bm} + u(t) \tag{18}$$

where P_{tar} (bar) and P_{out} (bar) are target outlet pressure and actual outlet pressure, respectively; $e(t)$ (bar) is the deviation; K_p, K_I and K_D are the PID control coefficients; $u(t)$ (V) is the change of control voltage; $v_{bm,new}$ (V) is the new control voltage after PID control. The parameters of the simulated hydrogen circulation pump are listed in Table 2.

2.1.3. Pipeline model

The pressure drop and dynamic response lag caused by gas transfer inside the pipeline is considered in this model. Pressure loss includes local pressure loss and frictional pressure loss:

$$\Delta p = \Delta p_m + \Delta p_f \tag{19}$$

$$\Delta p_m = \frac{1}{A_{pip}} \left(m_{out} u_{out} - m_{in} u_{in} \right) \tag{20}$$

$$\Delta p_f = \frac{2 C_f L \rho_{ave} (u_{ave})^2}{\delta_{pip}} \tag{21}$$

$$C_f = \begin{cases} 16 Re^{-1}, & Re \le 2000; \\ 0.079 Re^{-0.25}, & Re \ge 4000. \end{cases} \tag{22}$$

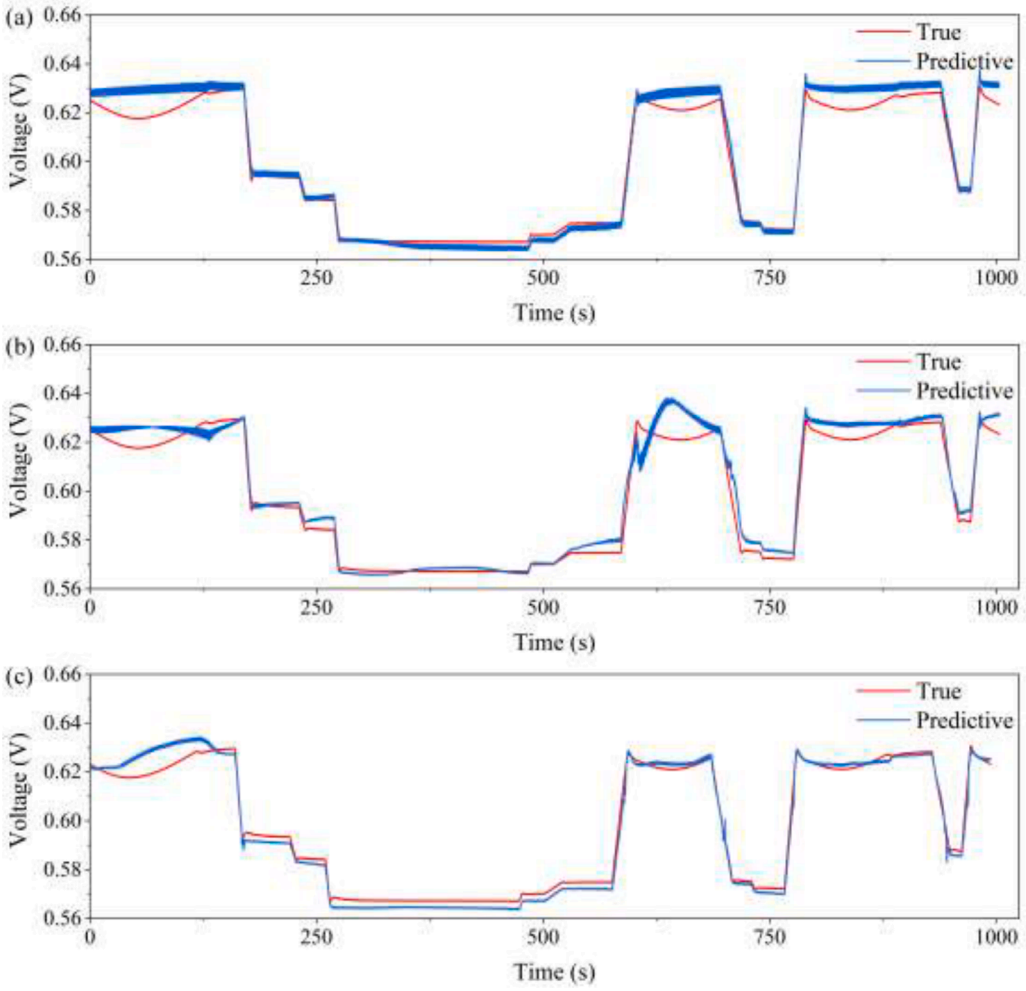

Fig. 7. Prediction results of single cell output voltage in operating condition 1: (a) MPR, (b) SVR, (c) LSTM-MLP.

$$Re = \frac{\rho_g u_g \delta_{pip}}{\mu_g} \tag{23}$$

$$\rho_g = \frac{P_g}{RT}\left(\sum_i M_i X_i\right) \tag{24}$$

$$\mu_g = \sum_i \frac{X_i \mu_i}{\sum_j X_j \phi_{ij}}, \phi_{ij} = \frac{\left[1 + \left(\frac{\mu_i}{\mu_j}\right)^{0.5}\left(\frac{M_j}{M_i}\right)^{0.25}\right]^2}{\left[8\left(1 + \frac{M_i}{M_j}\right)\right]^{0.5}} \tag{25}$$

where Δp (Pa) is the total pressure loss; Δp_m (Pa) is the local pressure loss; Δp_f (Pa) is the frictional pressure loss; A_{pip} (m^2) is the cross-sectional area of the pipeline; m_{out} (kg s^{-1}) and m_{in} (kg s^{-1}) are the mass flowrate into and out of the pipeline, respectively; u_{out} (m s^{-1}) and u_{in} (m s^{-1}) are the velocities into and out of the pipeline, respectively; C_f is the friction factor; L (m) is length of the pipeline; ρ_{ave} (kg m^{-3}) is the average density; u_{ave} (m s^{-1}) is the average flow rate; δ_{pip} (m) is the hydraulic diameter of the pipeline; Re is the Reynolds number; μ (kg m^{-1} s^{-1}) is the dynamic viscosity; M (g mol^{-1}) is the molar weight of gas species; X is the molar fraction of gas species. The response lag of the pipeline is reflected in the transmission time of gas in the pipeline:

$$t_{pip} = \frac{L}{u_{ave}} \tag{26}$$

where t_{pip} (s) is the transmission time of gas in the pipeline.

The development of other sub-models of air compressor, membrane humidifier, and radiator can be found in our previous works [24].

2.2. Prediction model

2.2.1. LSTM

Recurrent neural networks (RNNs) are a class of neural networks designed for processing the sequence data. Most RNNs can process variable length sequences. However, typical RNNs are prone to exploding gradient and vanishing gradient in training, which leads to the inability to deal with long sequences. In order to solve these problems, Hochreiter and Schmidhuber [25] improved RNN and designed the LSTM neural network model. Introducing the idea of self-cycling to generate a path where gradients flow continuously for a long time is a core contribution of the LSTM model. Fig. 2 shows the schematic of the LSTM model. The core concepts of LSTM could be described by the cell state, two activation functions, and three gates, and Fig. 3 shows schematic of the core concepts of LSTM.

The cell states run through the top of Fig. 3, with only a few linear interactions, conveying relevant information in the sequence chain.

The two activation functions are "tanh" and "σ" in Fig. 3, respectively.

$$\tanh(x) = \frac{e^x - e^{-x}}{e^x + e^{-x}} \tag{27}$$

$$\sigma(x) = \frac{1}{1 + e^{-x}} \tag{28}$$

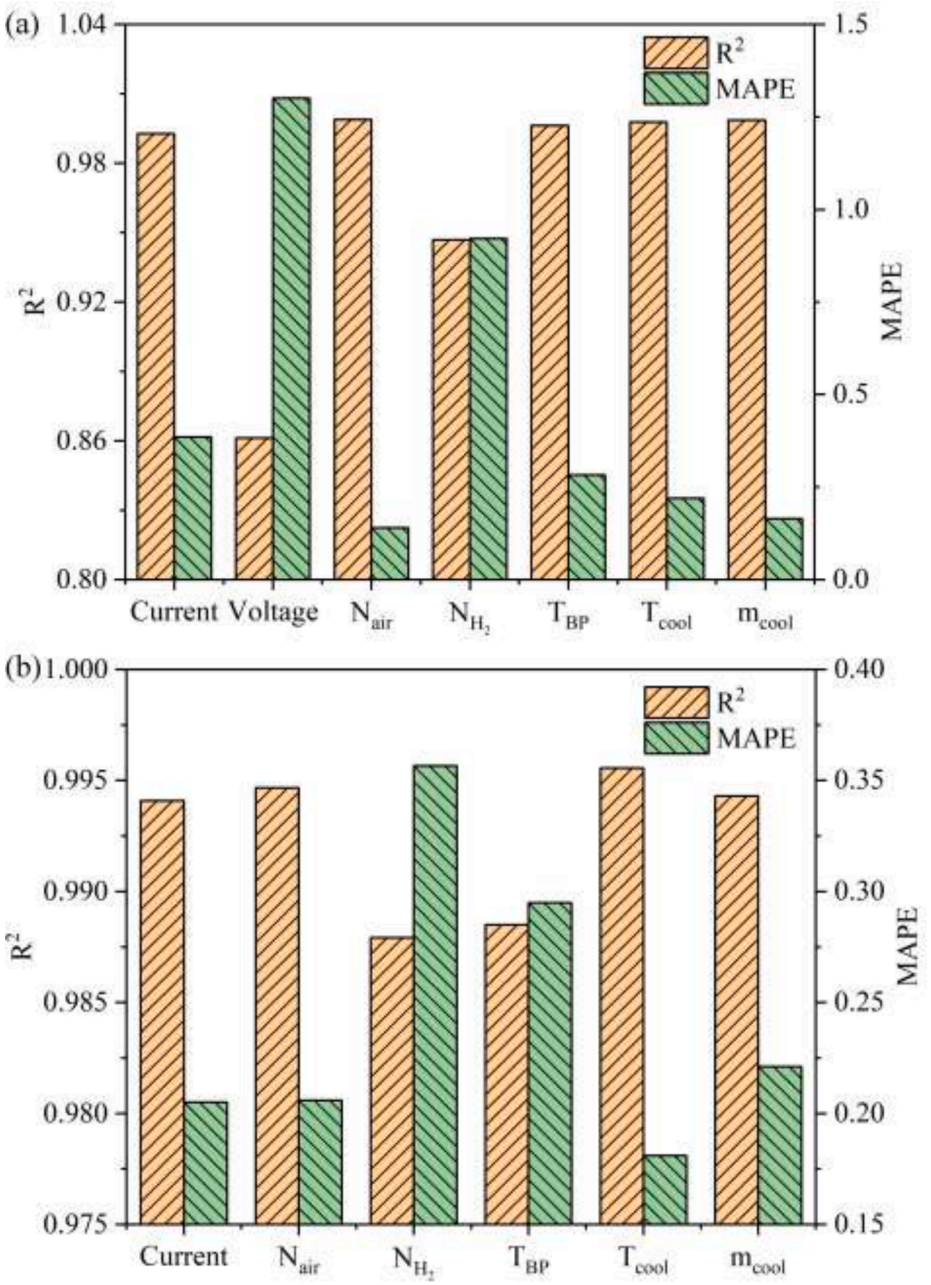

Fig. 8. Predictive performance of the model after removing a single feature for predicting (a) ASR, (b) single cell output voltage.

The three gates of LSTM are forget, input and output gates. The first is the forget gate, which determines what information should be discarded or retained:

$$f_t = \sigma\left(W_i^f x_t + b_i^f + W_h^f h_{t-1} + b_h^f\right) \tag{29}$$

where f_t is the current forget gate; W_i^f and W_h^f are the weights of the current forget gate; b_i^f and b_h^f are the biases of the current forget gate; x_t is the current input vector; h_{t-1} is the hidden state of the last LSTM cell output. The second is the input gate, which is used to update cell state:

$$i_t = \sigma\left(W_i^i x_t + b_i^i + W_h^i h_{t-1} + b_h^i\right) \tag{30}$$

$$c_t = f_t c_{t-1} + i_t \tanh\left(W_i^c x_t + b_i^c + W_h^c h_{t-1} + b_h^c\right) \tag{31}$$

where i_t is the current input gate; W_i^i and W_h^i are the weights of the current input gate; b_i^i andb_h^i are the biases of the current input gate; c_t is the cell state of current LSTM cell; c_{t-1} is the cell state of last LSTM cell; W_i^c and W_h^c are the weights; b_i^c andb_h^c are the biases; $\odot$ is Hadamard product. The third is the output gate, which determines the output of the current LSTM cell:

$$o_t = \sigma\left(W_i^o x_t + b_i^o + W_h^o h_{t-1} + b_h^o\right) \tag{32}$$

$$h_t = o_t \tanh(c_t) \tag{33}$$

where o_t is the current output gate; W_i^o and W_h^o are the weights of the current output gate; b_i^o and b_h^o are the biases of the current output gate; h_t is the hidden state of the current LSTM cell output.

2.2.2. LSTM-MLP

In this study, the prediction parameters (ASR and output voltage of the PEMFC) are values, however, the outputs of LSTM, cell state c or hidden state h, are vectors. Thus, we need to convert the vector to a

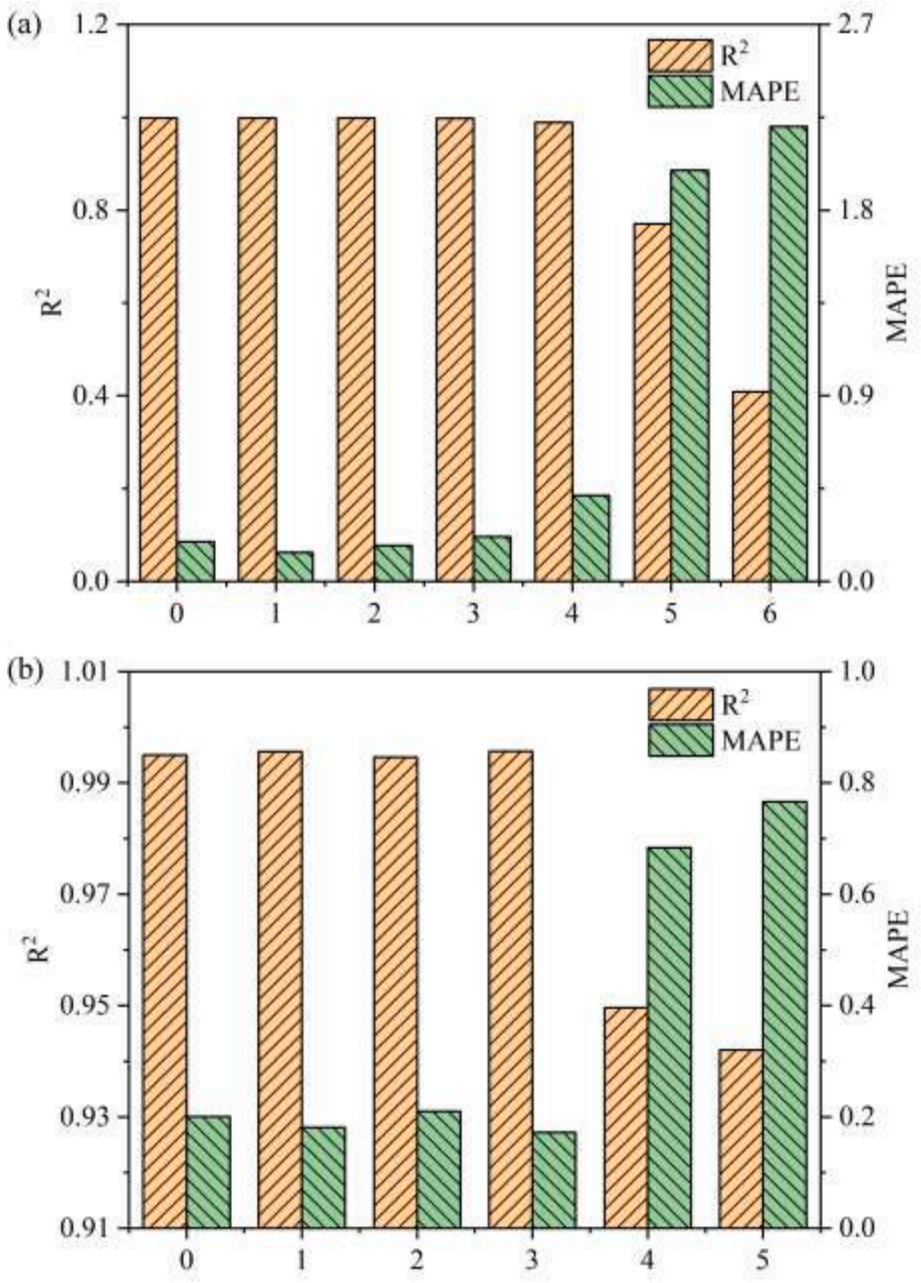

Fig. 9. Predictive performance of the model after removing multiple features for predicting (a) ASR, (b) single cell output voltage.

single value. We input the output of the hidden state of the last LSTM cell into the multilayer perceptron (MLP) with one neuron of the output layer, and the combined model is known as the LSTM-MLP. The input of LSTM is the sequence data of 100 consecutive sampling points, and the truth value is the ASR or output voltage of the last sampling point. The initial number of layers of LSTM is 1, the number of neurons in hidden layer is 8, and the direction is unidirectional. We use the two independent models to train and predict ASR and voltage, respectively, instead of using a multi-output model for the better predictive performance and training efficiency. The learning rate is 0.001, and the number of training epochs is within 2400. The mean square error (MSE) is set as the loss. Adam optimizer is used so that the learned gradient is adaptively corrected during the training. The training process of the LSTM-MLP is done by using the PyTorch library of the interpreted programming language Python.

2.3. Data acquisition

2.3.1. Random conditions generation

We use stochastic methods combined with reasonable constraints to generate the simulated automotive PEMFC operating conditions as the basic data. The range extender fuel cell hybrid vehicle is assumed in this study, and thus the automotive PEMFC system works in the relatively comfortable and high-efficient state without much excessive volatility. The maximum acceleration of the PEMFC system for loading and unloading is set as 0.03 A cm^{-2} s^{-1}, and the minimum and maximum current densities are set as 0.5 A cm^{-2} and 0.7 A cm^{-2}, respectively, that meet the fluctuation rate and range [26,27]. The random number is used to determine the state (loading or unloading) and acceleration of the PEMFC system at a certain moment. The whole operation time is limited to no less than 5000 s, and the final operating condition is the minimum current density. Fig. 4 shows the five random operating conditions generated under the above restriction framework.

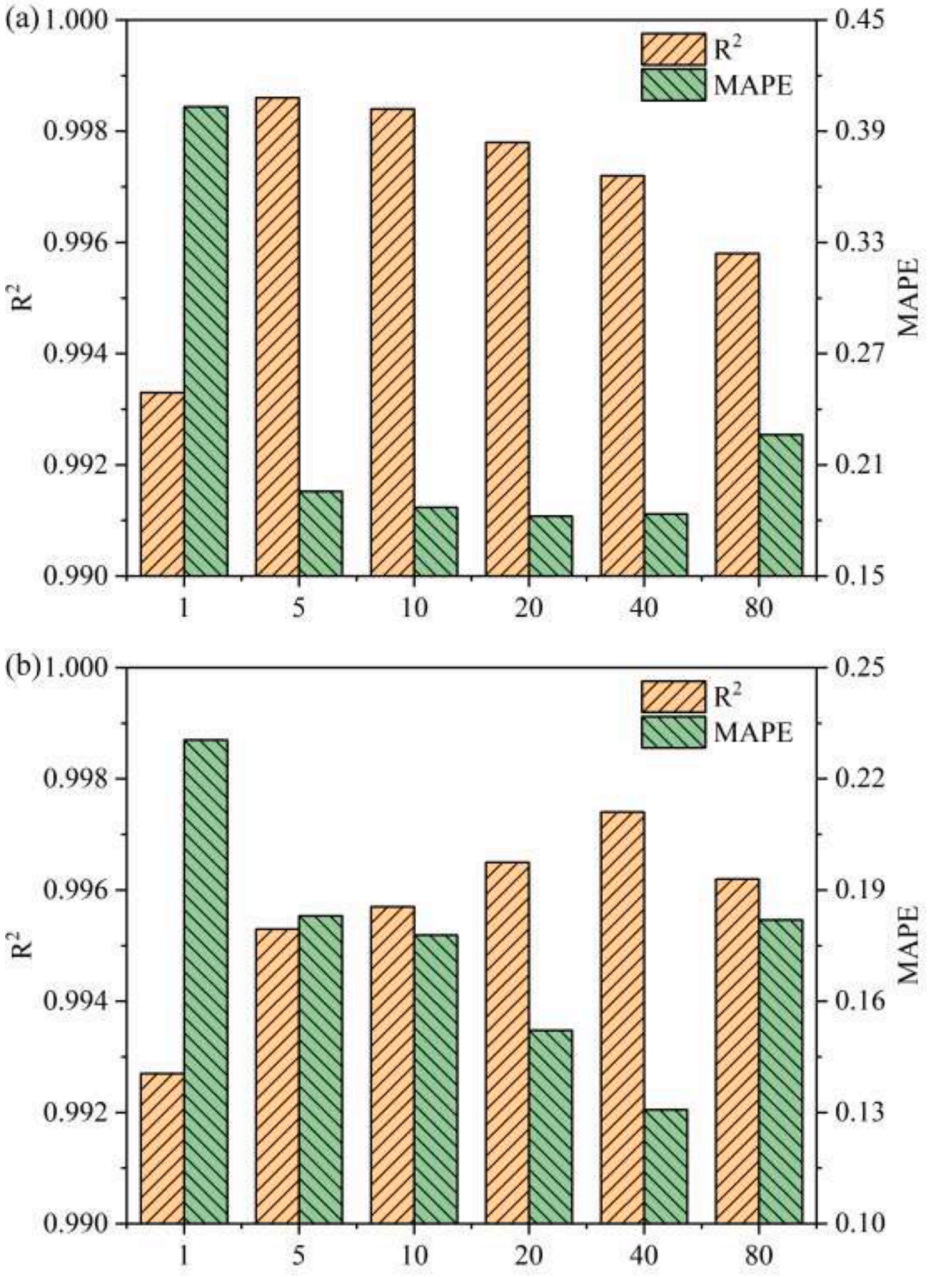

Fig. 10. Predictive performance of models using different sequence data durations: (a) ASR, (b) single cell output voltage.

2.3.2. Input features selection

To imitate the real operating environments of automotive PEMFC, we choose the physical quantities that can be measured or should be concerned in the vehicle to form the dataset, including current density, single cell output voltage, air compressor rotational speed, hydrogen circulation pump rotational speed, bipolar plate temperature, coolant outlet temperature, coolant flow rate and ASR. For predicting the ASR or output voltage, the residual parameters are set as the input features. Fig. 5 shows the variation curves of each feature in the data set obtained by sampling at operating condition 1 with time.

3. Results and discussion

3.1. Test criteria

We introduce four test criteria to evaluate the prediction performance: (1) coefficient of determination (R^2), (2) mean absolute error (MAE), (3) root mean square error (RMSE), (4) mean absolute percentage error (MAPE). The value range of R^2 is [0, 1], and the value range of other criteria is $[0, +\infty)$. The value of R^2 closing to 1, and that of other criteria closing to 0 indicate the better prediction performance.

$$R^2 = 1 - \frac{\sum_{i=1}^{n}(y_i - \hat{y}_i)^2}{\sum_{i=1}^{n}(y_i - \bar{y})^2} \tag{34}$$

$$MAE = \frac{1}{n}\sum_{i=1}^{n}|y_i - \hat{y}_i| \tag{35}$$

$$RMSE = \sqrt{\frac{1}{n}\sum_{i=1}^{n}(y_i - \hat{y}_i)^2} \tag{36}$$

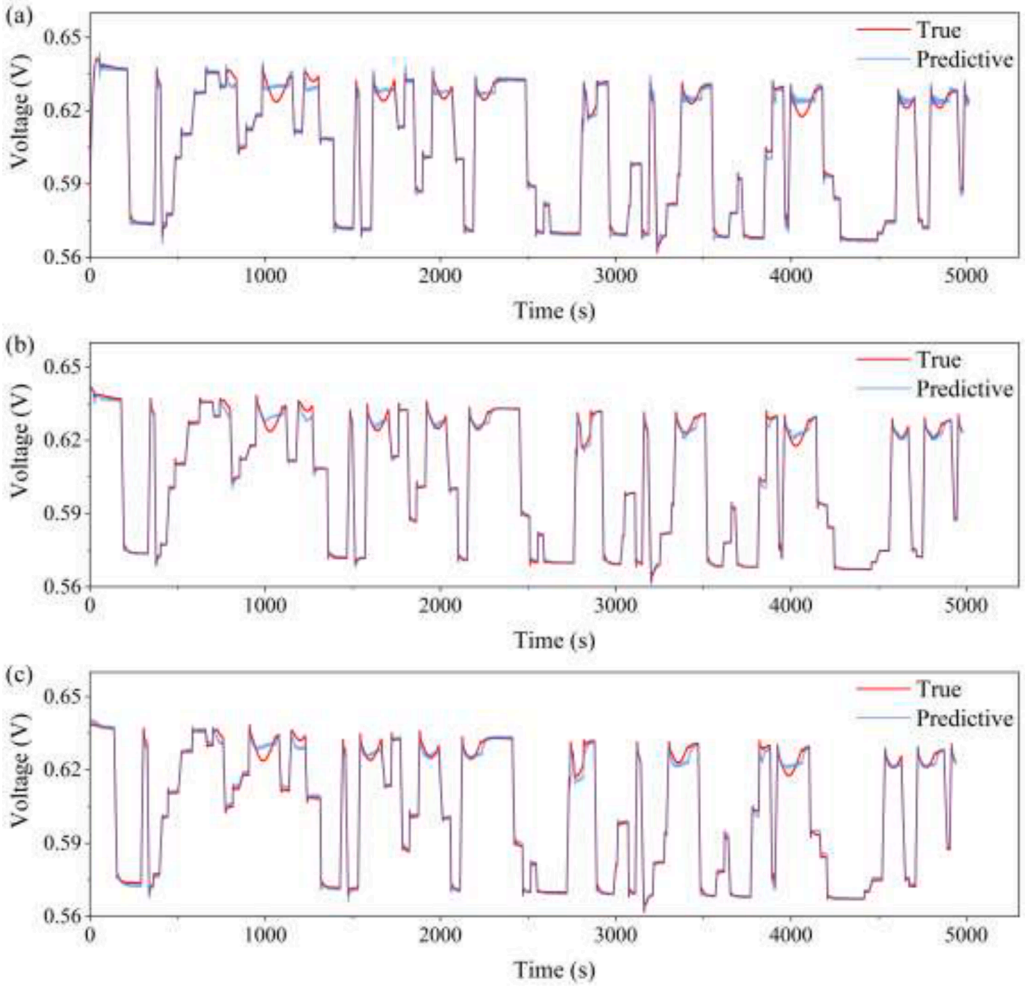

Fig. 11. Model prediction results of single cell output voltage with different sequence data duration: (a) 5 s, (b) 40 s, (c) 80 s.

$$\mathrm{MAPE} = \frac{1}{n}\sum_{i=1}^{n}\left|\frac{y_i - \hat{y}_i}{y_i}\right| \times 100\% \tag{37}$$

where $\bar{y}$ is the average value of the true value; n is the number of samples; y_i is the true value; $\hat{y}_i$ is the predicted value.

3.2. Comparative prediction performance of algorithms

We compare the prediction performance of LSTM-MLP with that of other commonly used regression algorithms, namely MPR and support vector regression (SVR). In order to save computing time and resources, we use operating condition 1 as the representative for the data set and divide it into train set, validation set and test set according to the ratio of 3:1:1. Table 3 shows the performance of ASR and single cell output voltage predicted by the three algorithms, respectively. The prediction results of ASR and single cell output voltage in test set of operating condition 1 by the three prediction algorithms are shown in Figs. 6 and 7, respectively. The results show that LSTM-MLP is more accurate in predicting both ASR and single cell output voltage than other algorithms.

The prediction accuracy of the three algorithms on predicting single cell output voltage does not show obvious difference, because the voltage depends mainly on the current density at each moment. However, there exist great differences in predicting ASR. The prediction accuracy of LSTM-MLP is significantly higher than that of MPR and SVR, because ASR is closely related to the membrane water content, and the water transport rate in the PEM is relatively slow compared to the change rate of the operating condition. Therefore, the membrane water content is not only related to the current operating condition, but also greatly affected by the historical states, with a time lag effect. Therefore, LSTM-MLP, which can remember historical data, is obviously more suitable than other algorithms for predicting ASR.

3.3. Network structure optimization

In following sections, the dataset is based on operating condition 1 as test set, operating condition 2 as validation set, and operating conditions 3, 4, and 5 as train set. In this section, the network structure of LSTM-MPL is optimized, and we design five neural networks:

"8–1″: the neuron number of hidden layer of LSTM is 8, and the MPL doesn't have hidden layer (only have input and output layers).
"8–8–1″: the neuron number of hidden layer of LSTM is 8, and the MPL has one hidden layer with the neuron number of 8.
"16–8–1″: the neuron number of hidden layer of LSTM is 16, and the MPL has one hidden layer with the neuron number of 8.
"32–8–1″: the neuron number of hidden layer of LSTM is 32, and the MPL has one hidden layer with the neuron number of 8.
"64–32–8–1″: the neuron number of hidden layer of LSTM is 64, and the MPL has two hidden layers with the neuron numbers of 32 and 8, respectively.

The prediction performance is shown in Table 4. As the network structure becomes complex, the prediction accuracy increases firstly

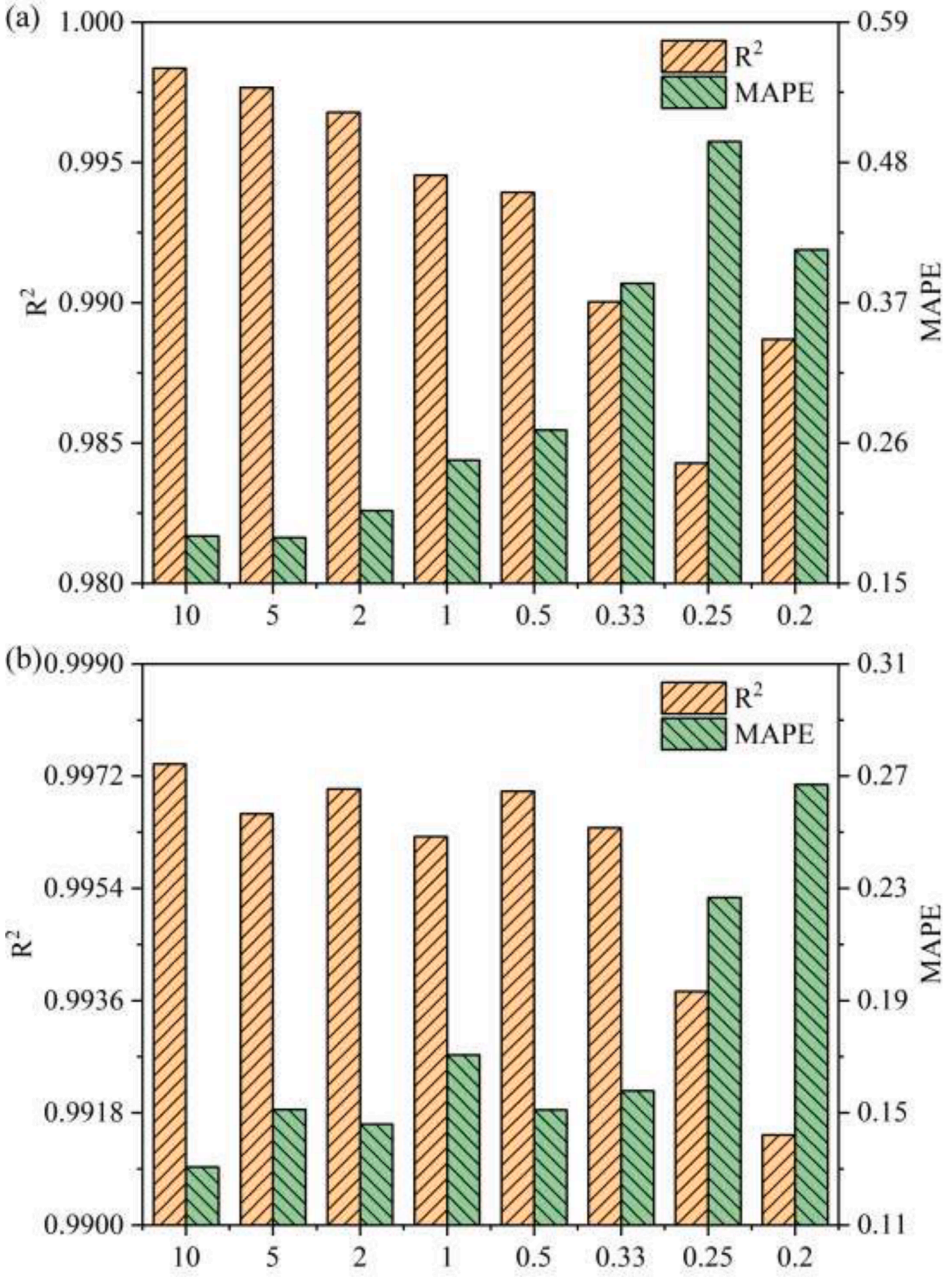

Fig. 12. Predictive performance of models using different sampling frequency: (a) ASR, (b) single cell output voltage.

with very limited improvement, and then even decreases. On the contrary, the complex model will cost much computation for the training, and increase uncertainty and decrease generalization for the prediction. Thus, we choose a balance result between prediction accuracy and model complexity, and use "8–8–1″ for the following study.

3.4. Feature sensitivity analysis

Due to the limited computing power and memory size of the chip, especially when it needs to be loaded in the vehicle controller, it is necessary to strictly limit the model complexity and data size. After reducing the input features, the amount of data will be reduced in proportion and the complexity of the model will be reduced accordingly. Therefore, how to effectively screen features is a very worthy direction. In this section, we make a sensitivity analysis of the input features and use this as a basis for feature selection. We train, validate, and test the model using a dataset with individual features removed. Fig. 8 shows the predictive performance of the model after removing one single feature. The larger R^2 and smaller MAPE indicates better prediction performance. When we remove a feature, if the training yields a worse model, it means that the feature is more sensitive to the output parameter.

As shown in Fig. 8, the coolant flow rate, coolant outlet temperature and air compressor rotational speed are the three insignificant features for both predicting ASR and single cell output voltage. In our simulated cases, the applied automotive PEMFC system model only simulates the normal working states, and the stack temperature is controlled in a stable state without the wild fluctuation by adjusting the coolant flow rate, that leads to the appearance that the changes of coolant flow rate and coolant temperature have little effect on the state of the stack. However, the temperature and coolant rate might become the significant features in the unnormal or fault states, where the stack temperature cannot be well controlled. For the air compressor rotational speed, the inlet pressure is constant as 2 bar, and the dynamic response of air compressor is fast. Under this condition, the air compressor rotational

speed is strongly related to the current density, and thus it shows similar information as the feature of current density. If the inlet pressure changes with different current densities, the air compressor rotational speed will become more important. Only removing the current density could also lead to a relatively good predictive performance because this feature could be reflected by other features such as hydrogen circulation pump rotational speed due to the constant pressure and stoichiometry assumption.

As shown in Fig. 8(a), the most important feature for predicting ASR is the single cell output voltage, followed by the hydrogen circulation pump rotational speed and current density. Under the condition of constant current density, ASR has a linear relationship with ohmic loss, so the single cell output voltage is strongly correlated with ASR. Furthermore, when predicting ASR, it is very necessary to take the single cell output voltage as the input feature. The hydrogen circulation pump rotational speed corresponds to the amount of hydrogen and water vapor supply. Since the inlet pressure is constant as 2 bar, the amount of hydrogen supply represents the current density and reflects the operating conditions of the stack. The amount of water vapor supply directly corresponds to the humidification degree of PEMFC, which directly determines the membrane water content and ASR. As can be seen from Fig. 8(b), the most important feature for predicting the single cell output voltage is the hydrogen circulation pump rotational speed. As mentioned above, due to the constant inlet pressure, the hydrogen circulation pump rotational speed contains information such as current density, and PEM humidification degree, which have the direct impacts on the single cell output voltage.

In order to reduce the model complexity and data size as much as possible, remove as many features as possible under the condition of ensuring the prediction accuracy. According to the feature importance shown in Fig. 8, multiple features are removed cumulatively from small to large. Fig. 9 shows the predictive performance of the model after removing multiple features. After removing less than four insignificant features, it will not have much impact on the prediction performance of the model, and even slightly improve the prediction accuracy. This is because some features are not closely related to the target, resulting in a possible negative impact. If only one feature is used to predict the single cell output voltage, the R^2 is 0.9420 and MAPE is 0.7662%. This indicates that the single cell output voltage is strongly related to a single feature and is strongly affected by a single condition. Adding other feature inputs will have limited improvement in prediction performance. Unlike the single cell output voltage, at least three features are required to be input to predict ASR in order to ensure that the R^2 value is higher than 0.9, which indicates that the ASR is greatly affected by a variety of conditions.

3.5. Sequence duration optimization

In the previous sections, the input is sequence data with 100 consecutive sampling points as a group and the sampling frequency is 10 Hz, and thus a sequence data spans 10 s. For the model development, the input sequence data duration can be treated as a hyperparameter. In this section, the effect of sequence duration on the prediction performance is discussed, and the sequence durations are selected as 1 s, 5 s, 10 s, 20 s, 40 s, and 80 s, respectively. In terms of data set, the three insignificant features discussed in the previous section are eliminated.

Fig. 10 shows the predictive performance of models using different sequence data durations. The results show that the accuracy of model prediction of ASR and single cell output voltage firstly increases and then decreases with increasing sequence data duration. The optimal sequence data duration for predicting ASR is 5 s (R^2) or 20 s (MAPE), and that for predicting single cell output voltage is 40 s. The reason is that too short sequence data duration contains too little time sequence information, so that the model makes prediction without enough information, resulting in low accuracy. However, too long sequence data duration contains too much time sequence information, that also has a negative effect on the prediction and leads to low accuracy.

Fig. 11 shows the model prediction results of single cell output voltage with different sequence data duration. The obvious errors mainly occur at the overshot and undershot phenomenon when the current density changes. In order to accurately capture the voltage change at the overshot and undershot phenomenon, the input data should include the characteristics of current density change processes that explain why the optimal sequence data is 40 s for predicting the single cell output voltage.

3.6. Sampling frequency optimization

When the sequence data duration is constant, the data size and computation amount of developing the model can be effectively reduced by reducing the sampling frequency. Thus, the sampling frequency should be reduced as far as possible under the condition of ensuring the prediction accuracy. In this section, the effect of sampling frequency on the prediction performance is discussed, and the sampling frequencies are selected as 10 Hz, and 5 Hz, 2 Hz, 1 Hz, 0.5 Hz, 0.33 Hz, 0.25 Hz and 0.2 Hz, respectively. The three insignificant features are eliminated, and the sequence data durations for predicting ASR and single cell output voltage are 20 s and 40 s, respectively.

Fig. 12 shows the predictive performance of models using different sampling frequencies. For predicting ASR, the prediction accuracy decreases slowly with the decline of sampling frequency. When the sampling frequency drops to 0.5 Hz, the R^2 still reaches 0.9939 and MAPE is only 0.2702%. This reduces the data size and computation amount by 0.05 times compared to that of 10 Hz. There is no obvious regularity in predicting the single cell output voltage. Sampling frequency of 0.25 Hz is an appropriate choice for predicting single cell output voltage.

4. Conclusion

To monitor the health status of fuel cell stacks during operation, the dynamic process of ASR and output voltage are the main two indexes. In this study, a transient model of PEMFC system is built to simulate the dynamic process of the automotive PEMFC, and the random operating conditions are loaded to generate the data. The data set is used to train the data-driven model. The results show that the LSTM-MLP is more accurate in predicting both ASR and single cell output voltage than the benchmark algorithms (MPR and SVR), because the target value is not only related to the current conditions, but also affected by the historical conditions, with a time lag effect. In order to reduce the data size and model complexity, a sensitivity analysis of the input features is performed and three insignificant features are selected for both predicting ASR and output voltage. The prediction performance even slightly improves after removing the three insignificant features. Predicting the ASR is greatly affected by multiple physical quantities, however, predicting the single cell output voltage is strongly related to one single physical quantity. The optimal sequence data duration for predicting ASR is 5 s or 20 s, and that for predicting single cell output voltage is 40 s in this study. Moreover, the sampling frequency can be reduced to 0.5 Hz for predicting ASR and 0.25 Hz for predicting single cell output voltage that could reduce the computation amount and data volume by 0.025 to 0.05 times.

Declaration of Competing Interest

The authors declare that they have no known competing financial interests or personal relationships that could have appeared to influence the work reported in this paper.

Data availability

Data will be made available on request.

Acknowledgements

This research is supported by the National Natural Science Foundation of China (No. 52176196), the National Key Research and Development Program of China (No. 2022YFE0103100), the China Postdoctoral Science Foundation (No. 2021TQ0235), and the Hong Kong Scholars Program (No. XJ2021033).

References

[1] Cheng C, Wang S, Wu Y, et al. Thermally regenerative CO2-induced pH-gradient cell for waste-to-energy conversion. ACS Energy Lett 2021;6(9):3221–7.
[2] Liu Z, Sun Y, Xing C, et al. Artificial intelligence powered large-scale renewable integrations in multi-energy systems for carbon neutrality transition: challenges and future perspectives. Energy and AI 2022;10:100195.
[3] Jiao K, Wang B, Du Q, et al. Water and thermal management of proton exchange membrane fuel cells. Elsevier; 2021. https://doi.org/10.1016/B978-0-323-91116-0.00005-5.
[4] Moon S, Lee YJ, Lee DJ. A cost-effectiveness analysis of fuel cell electric vehicles considering infrastructure costs and greenhouse gas emissions: an empirical case study in Korea. Energy Technol Assessments 2022;54:102777.
[5] Yang Z, Wang B, Jiao K. Life cycle assessment of fuel cell, electric and internal combustion engine vehicles under different fuel scenarios and driving mileages in China. Energy 2020;198:117365.
[6] Xu Y, Yang Z, Jiao K, et al. Development of a comprehensive transient fuel cell-battery hybrid system model and rule-based energy management strategy. Int J Green Energy 2022. https://doi.org/10.1080/15435075.2022.2119856.
[7] Wang Z, Tongsh C, Wang B, et al. Operation characteristics of open-cathode proton exchange membrane fuel cell with different cathode flow fields. Energy Technol Assessments 2022;49:101681.
[8] Jiao K, Xuan J, Du Q, et al. Designing the next generation of proton-exchange membrane fuel cells. Nature 2021;595:361–9.
[9] Kheirandish A, Motlagh F, Shafiabady N, et al. Dynamic modelling of PEM fuel cell of power electric bicycle system. Int J Hydrogen Energy 2016;41(22):9585–94.
[10] Qin Z, Wu K, Wu S, et al. Investigation of assisted heating cold start strategies from -40°C for proton exchange membrane fuel cell stack. Int J Green Energy 2023. https://doi.org/10.1080/15435075.2022.2163590.
[11] Zhang G, Xie B, Bao Z, et al. Multi-phase simulation of proton exchange membrane fuel cell with 3D fine mesh flow field. Int J Energy Res 2018;42(15):4697–709.
[12] Xie B., Zhang G., Jiang Y., et al. "3D+1D" modeling approach toward large-scale PEM fuel cell simulation and partitioned optimization study on flow field. eTransportation, 2020, 6: 100090.
[13] Chen H, Shan W, Zhang T, et al. Study on the influence of segmented fuel cell by grooving method and its application in oxygen starvation diagnosis. Int J Hydrogen Energy 2022;47(2):1267–78.
[14] Xia L, Xu Q, He Q, et al. Numerical study of high temperature proton exchange membrane fuel cell (HT-PEMFC) with a focus on rib design. Int J Hydrogen Energy 2021;46(40):21098–111.
[15] Wang B, Zhang G, Wang H, et al. Multi-physics-resolved digital twin of proton exchange membrane fuel cells with a data-driven surrogate model. Energy and AI 2020;1:100004.
[16] Niu T, Huang W, Zhang C, et al. Study of degradation of fuel cell stack based on the collected high-dimensional data and clustering algorithms calculations. Energy and AI 2022;10:100184.
[17] Wang Y, Wu K, Zhao H, et al. Degradation prediction of proton exchange membrane fuel cell stack using semi-empirical and data-driven methods. Energy and AI 2023;11:100205.
[18] Wang B, Xie B, Xuan J, et al. AI-based optimization of PEM fuel cell catalyst layers for maximum power density via data-driven surrogate modeling. Energy Conversion and Manag 2020;205:112460.
[19] Qiu Y, Wu P, Miao T, et al. An intelligent approach for contact pressure optimization of PEM fuel cell gas diffusion layers. Appl Sci 2020;10(12):4194.
[20] Li H, Xu B, Lu G, et al. Multi-objective optimization of PEM fuel cell by coupled significant variables recognition, surrogate models and a multi-objective genetic algorithm. Energy Conversion and Manag 2021;236:114063.
[21] Yang Z, Wang B, Sheng X, et al. An artificial intelligence solution for predicting short-term degradation behaviors of proton exchange membrane fuel cell. Appl Sci 2021;11(14):6348.
[22] Wang B, Wu K, Yang Z, et al. A quasi-2D transient model of proton exchange membrane fuel cell with anode recirculation. Energy Conversion and Manag 2018;171:1463–75.
[23] Zhang Q, Tong Z, Tong S, et al. Modeling and dynamic performance research on proton exchange membrane fuel cell system with hydrogen cycle and dead-ended anode. Energy, 2021;218:119476.
[24] Yang Z, Du Q, Jia Z, et al. A comprehensive proton exchange membrane fuel cell system model integrating various auxiliary subsystems. Appl Energy 2019;256:113959.
[25] Hochreiter S, Schmidhuber J. Long short-term memory. Neural Comput 1997;9(8):1735–80.
[26] Desantes JM, Novella R, Pla B, et al. Effect of dynamic and operational restrictions in the energy management strategy on fuel cell range extender electric vehicle performance and durability in driving conditions. Energy Conversion and Manag 2022;266:115821.
[27] Zeng T, Zhang C, Hu M, et al. Modelling and predicting energy consumption of a range extender fuel cell hybrid vehicle. Energy 2018;165(Part B):187–97.